3D Adaptive AUV Sampling for Classification of Water Masses

Yaolin Ge[1], Jo Eidsvik[1], and Tore Mo-Bjørkelund[2]

[1]Department of Mathematical Sciences, Norwegian University of Science and Technology, Trondheim, Norway

[2]Department of Marine Technology, Norwegian University of Science and Technology, Trondheim, Norway

Abstract

Autonomous underwater vehicles with onboard computing units foster innovative approaches for sampling oceanographic phenomena. Feedback of observations via the onboard model to planning algorithms enable adaptive sampling for such robotic units. In this work we develop, implement and test an adaptive sampling algorithm for efficient sampling of water masses in a three-dimensional frontal system. Focusing on a river plume, salinity variations are used to characterize the water masses. A threshold in salinity is assumed to distinguish the ocean and river waters, so that excursions below the threshold define river waters. The onboard model builds on a Gaussian random field representation of the salinity variations in (north, east, depth) coordinates. This model is initially trained from numerical ocean model data, and then updated with data gathered by the vehicle sensor. The Gaussian random field model further allows closed-form expressions of the expected spatially integrated Bernoulli variance of the salinity excursion set, which is used to reward sampling efforts. Combining these results with forward-looking planning algorithms, we suggest a workflow for three-dimensional adaptive sampling to map river plume systems. Simulation studies are used to compare the suggested approach with others. Results of field trials in the Nidelva river plume in Norway are then presented and discussed.

Index Terms

AUV, adaptive sampling, path planning, excursion sets, river plume

yaolin.ge@ntnu.no
jo.eidsvik@ntnu.no
tore.mo-bjorkelund@ntnu.no

I. INTRODUCTION

A river plume is formed when the fresh water flowing out of the river encounters the saline water in the ocean [1]. When these two different water masses meet, they form a varying spatio-temporal boundary [2]. There have been increasing efforts using numerical models and data to investigate such phenomena in the past decades [3, 4, 5, 6, 7, 8].

Autonomous underwater vehicles (AUVs) with onboard sensors and computing resources provide rich opportunities for oceanographic sampling as they can calibrate numerical ocean model outputs with in-situ data, and fill in the sampling resolution gaps at locations with large uncertainty [9, 10, 11, 12]. For frontal regions such as river plumes, AUV sampling is helpful for classifying the different water masses more accurately. Previous AUV sampling efforts focus mainly on pre-programmed designs [13] or use event-triggered adaptation of designs [14, 15]. Recent efforts have shown added value of having model-based adaptive sampling plans [16]. Adaptive sampling strategies here refer to AUV planning schemes that enable the AUV plan to be updated based on the posterior knowledge from in-situ sampling and the probabilistic model description. Ideas from statistical sampling design are highly useful in this field, because they can help guide the AUV to informative locations [16, 17].

The main contribution of this work is a three-dimensional (3D) full-scale adaptive AUV sampling strategy. With the AUVs limiting computing resources, a Gaussian random field (GRF) model serves as a statistical proxy models for the spatial salinity field in the 3D domain (north, east, depth). This 3D GRF model running onboard the AUV is sequentially refined using in-situ observations. This refined probabilistic model is further a basis for evaluating AUV sampling designs. Starting with prior knowledge from a numerical ocean model, we use an AUV to adaptively explore the 3D boundary between the water masses in the river plume. We suggest algorithms to speed up design computations and to enable efficient robotic maneuverability [18]. We use a statistical design criterion based on the uncertainty of the Excursion Set (ES) of low salinity which distinguishes the river from the ocean water. This ES is defined by spatial locations having salinity level below a user-defined threshold. Building on recently developed closed form expressions [16] for the Expected Integrated Bernoulli Variance (EIBV) associated with the ES, we compare the EIBV associated with each candidate design location, and select the design which has the minimum EIBV. The EIBV is a useful criterion for improved classification of the river plume as it is large when probabilities of excursions are far from 0 and 1. One should select sampling designs that on expectation pull probabilities towards the 0 and 1 end-points to reduce the uncertainty of the ES.

Via simulation studies and *in-situ* measurements from the Nidelva river plume in Trondheim, Norway, we study the properties of the EIBV sampling plans in the 3D domain. For the real-world experiments we used a Light AUV (LAUV) [19] with an on-board NVIDIA Jetson TX2 computing unit.

This paper is structured as follows. In Section II we provide the background and motivation for our work on adaptive AUV sampling to river plume water masses characterization. In Section III we introduce the models and methods used in this paper. In Section IV we present our implementation used for path planning. In Section V we show a simulation study illustrating the properties of our 3D adaptive sampling approaches. In Section VI we show results from the Nidelva river plume experiments. In Section VII we summarize our main contributions and findings and point to future work.

II. Ocean sampling

A. Data sources

Numerical solutions of the complex differential equations governing spatio-temporal oceanographic variation with boundary conditions and forcing are essential in understanding the ocean variability. In our application we rely on a fjord-scale implementation of the SINMOD software [20]. Such ocean model data provide physical interpretability of the ocean variability, but they often need calibration or bias adjustments, and there have been growing interests in uncertainty quantification and data assimilation methods for various scales of this challenge, see e.g. [21].

Traditional *in-situ* measurements generating input or calibration data to numerical ocean models include stationary or floating buoys, gliders, moorings and ships [22]. With the advent of smaller inexpensive sensor systems, one has capabilities of handling a variety of measurements for biological, chemical and oceanographic purposes [22]. Ships data can be expensive, and buoys and gliders have limited flexibility in maneuverability given coverage constraints [23].

Satellite imagery has been a powerful and useful tool for analyzing ocean variables. Data from satellites can provide a large-scale coverage of the entire field of interest, and even output portraits of river plumes [6]. However, due to large latency and uncertainty (cloud coverage issues) of obtaining such images, the usage of satellite imagery is limited. Satellite data unfavorably cover only the surface of the ocean [24].

The development of underwater robotics have led to a large number of robot-assisted applications in oceanography. Thanks to the flexibility of the robots, there are growing numbers of autonomous sampling missions which are conducted by robots [9]. Benefits further include real-time sensing and high-resolution data gathering, with large opportunities to move in flexible paths in the ocean environment. In our case, an AUV is used as the target platform which is able to support 3D adaptive sampling at high resolution.

B. Sequential AUV sampling

We denote the salinity field by $\{\xi_{\boldsymbol{u}}; \boldsymbol{u} \in \mathcal{M} \subset \mathcal{R}^3\}$, where the location $\boldsymbol{u}$ is (longitude, latitude, depth) and $\mathcal{M}$ is the spatial domain of interest. Initially, we specify a probabilistic model for the salinity based on numerical ocean model data. This provides a realistic initial model for the 3D salinity characteristics, one that it is much more physically inspired than a simple linear regression from available in-situ AUV data [16]. We still use regression analysis to calibrate the 3D ocean model data to the real-world ocean experiment by using a short preliminary AUV survey [25]. The objective of the survey is not to reveal the entire field, but rather provide some *in-situ* measurements to adjust the ocean-model data and to form a reasonable prior model for the day of deployment. Therefore, the path for the preliminary survey can be as simple as a transect line with yo-yo movements in the vertical direction. As mentioned in the previous section, one can also use satellite data or even drone images in this initial model specification, if such data are available [26].

In-situ salinity observations for the main part of the deployment are denoted by $\{\boldsymbol{y}_j; j = 1, \ldots, J\}$, for stages j of AUV measurements gathered over time. The vector $\boldsymbol{y}_j$ of measurements at stage j, holds N_j measurements made according to spatial sampling design $\boldsymbol{D}_j$. The initial deployment location will then define $\boldsymbol{D}_1$. We denote by $\mathcal{Y}_j = \{(\boldsymbol{y}_1, \boldsymbol{D}_1), \ldots, (\boldsymbol{y}_j, \boldsymbol{D}_j)\}$ the collection of data gathered with the selected designs up to stage j. Initially, this is an empty set; $\mathcal{Y}_0 = \emptyset$.

The sequential designs are selected adaptively based on what is evaluated to be the most informative AUV sampling locations. In this evaluation, the on-board model is conditional to all the data gathered until the current time. With new observations available, data assimilation methods are used to update the probabilistic representation for the salinity variables. This means that the model is 'alive', and changing at every stage, depending on the data. Adaptive sampling fits into the diagram loop in Fig. 1. In our setting the spatial design plan is optimized based on the current spatial statistical model. Then the AUV gathers new observations according to the chosen design, and the GRF model is updated. This continues over stages $j = 1, \dots J$.

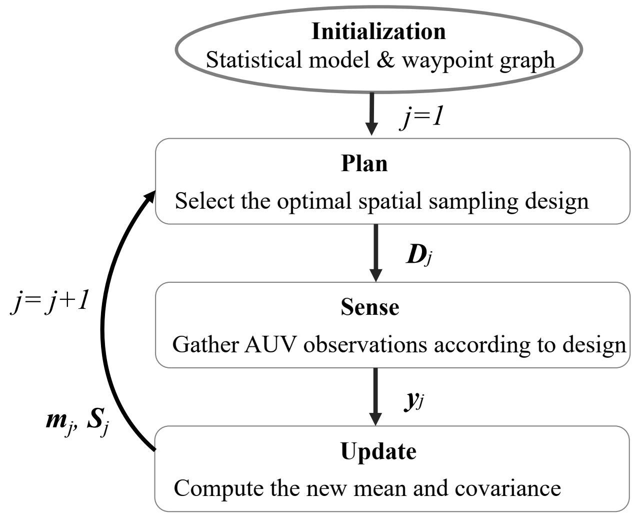

Fig. 1: Sequential loop where design $\boldsymbol{D}_j$ is chosen based on the updated model, $\boldsymbol{y}_j$ is the data collected in this design, and this is used to update the model ($\boldsymbol{m}_j$, $\boldsymbol{S}_j$). This continues over stages $j = 1, 2, \dots J$.

For prioritizing sampling efforts, one must impose an expected reward or value function associated with the different available sampling designs. At each stage, the expected rewards of all possible designs are evaluated. In our setting with river plumes, it makes sense to reward sampling locations that are expected to give data that improve the spatial characterization of the water masses [15, 16]. The setting is illustrated in Fig. 2, where we indicate the current location of the AUV, its path, and the sampling design opportunities at this stage. The information criterion (EIBV) is calculated for all feasible designs, shown as circular dots. Here, smaller dots with lighter colors are indicative of larger expected uncertainty reduction. The adaptive sampling approach would act by moving to the location with lowest EIBV.

III. Statistical Models and Methods for AUV sampling

We next discuss our probabilistic modeling choices for the salinity field, and show how this enables efficient data assimilation as well as onboard design criteria. We then define ES and the EIBV as a design criterion, and finally present an adaptive sampling design algorithm for efficient 3D characterization of the river plume.

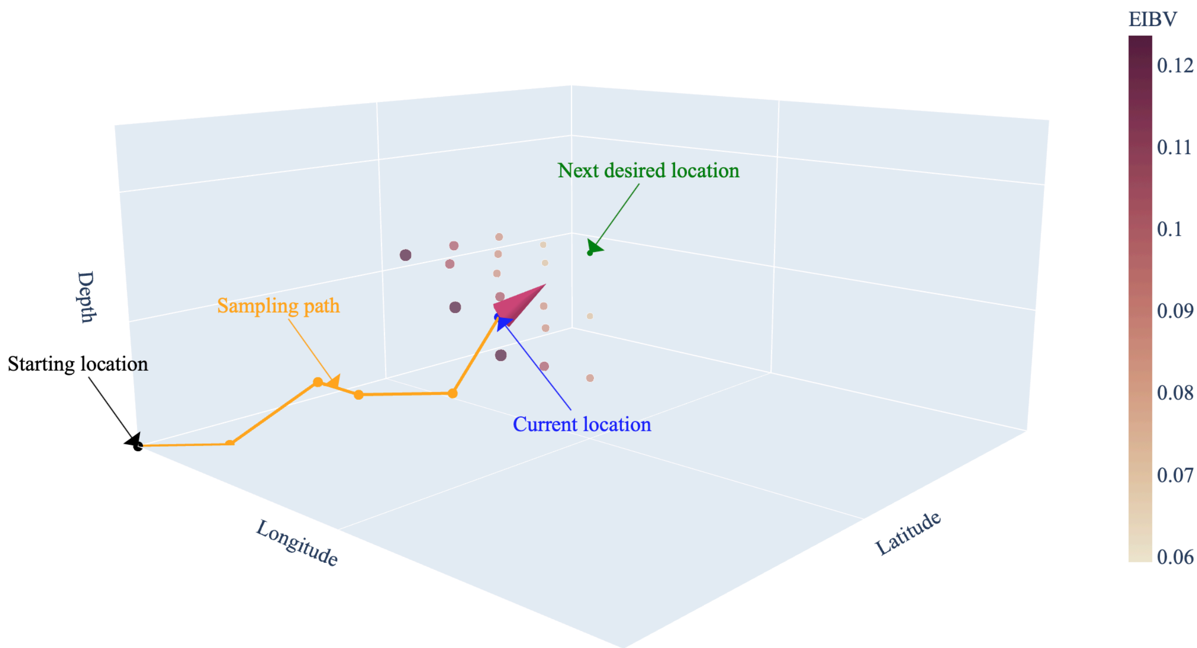

Fig. 2: An adaptive path example on a 3D waypoint graph. There are 17 candidate locations in different layers, the blue dot shows the current AUV location whereas the green dot indicates the desired next waypoint selected based on the minimum EIBV criterion.

A. *On-board computing with GRFs*

The prior model for river plume salinity $\{\xi_{\boldsymbol{u}}, \boldsymbol{u} \in \mathcal{M} \subset \mathcal{R}^3\}$, is defined via a GRF. A working assumption in our work is hence that the GRF provides a reasonable proxy model for the spatial salinity field in (latitude, longitude, depth). The initial model specification includes estimating the expected value of the field, its variability and spatial dependence. Note that the duration of the experiment will be short and the temporal variation in the river plume is ignored here. To check the Gaussian assumption, we made a quantile-quantile (QQ) plot from the SINMOD salinity data (Fig. 3). Here, we have computed the mean and variance at each location in a gridded domain over replicates of time steps. The standardized residuals are used in the QQ plot. The QQ plot in Fig. 3 shows a crossplot of the theoretical Gaussian quantile of the residuals against the empirical quantile of residuals in the data set. The blue line that we achieve is quite close to the straight line (red). Of course, the physical model does not give a Gaussian model, and we notice a sharper distribution near 0, but nevertheless the discrepancy is rather small.

Critically, the GRF model enables onboard data assimilation and adaptive AUV sampling

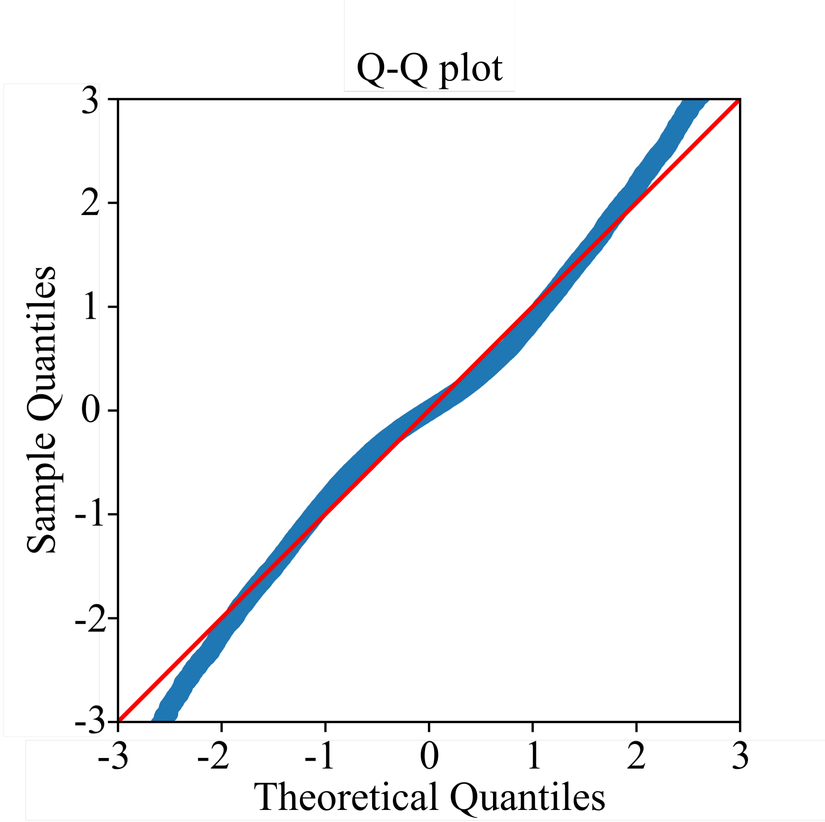

Fig. 3: Quantile-quantile plot of the residual based on SINMOD estimation. The residual is computed by subtracting the mean of the field and dividing the standard deviation.

efforts, as we will describe next. For onboard implementation and computing, the spatial domain is discretized to a set of n grid locations; $\{\boldsymbol{u}_1, \ldots, \boldsymbol{u}_n\}$. This grid is also used for the waypoint graph setting for the AUV sampling design. The prior or initial GRF model at these grid locations is denoted by

$$\boldsymbol{\xi} = (\xi_{\boldsymbol{u}_1}, \ldots, \xi_{\boldsymbol{u}_n})^T, \quad \boldsymbol{\xi} \sim N(\boldsymbol{\mu}, \boldsymbol{\Sigma}), \tag{1}$$

with associated probability density function (PDF) $p(\boldsymbol{\xi})$. Here, length-n vector $\boldsymbol{\mu}$ represents the prior mean of the 3D salinity variations, as will later be specified from ocean model data and a preliminary AUV transect run. The $n \times n$ covariance matrix $\boldsymbol{\Sigma}$ is defined via a Matérn covariance function with elements $\Sigma(i, i') = \sigma^2(1 + \phi_1 h(i, i')) \exp(-\phi_1 h(i, i'))$, where σ^2 is the variance and ϕ_1 a correlation decay parameter [27]. The distance between grid nodes $\boldsymbol{u}_i$ and $\boldsymbol{u}_{i'}$ is defined for east, north and depth Euclidean distances via $h^2(i, i') = h_E^2(i, i') + h_N^2(i, i') + (\phi_1^2/\phi_2^2)h_D^2(i, i')$, with h being distance, and subscripts E, N, D indicating each of the three directions in vector $\boldsymbol{u}_{i'} - \boldsymbol{u}_i$. Studies have shown that the lateral stretch of the river plume tends to be many magnitudes above the vertical stretch [1]. To model the correlation in different dimensions properly, we employ anisotropy between the lateral domain and the vertical domain. This means that the depth dimension is scaled differently (ϕ_2) using another correlation decay parameter than the one used in the lateral field (ϕ_1).

The measurements at each stage $j = 1, \ldots, J$ are modeled by a Gaussian likelihood model

$$\boldsymbol{y}_j|\boldsymbol{\xi} \sim N(\boldsymbol{F}_j\boldsymbol{\xi}, \boldsymbol{R}_j), \tag{2}$$

where $\boldsymbol{F}_j$ is an $N_j \times n$ selection matrix containing an entry of 1 in each row and 0 otherwise. The 1 entry refers to the sampling indices. With the covariance matrix $\boldsymbol{R}_j = r^2\boldsymbol{I}_{N_j}$, we assume that the data are conditionally independent, given the underlying salinity. Here, r indicates the measurement standard deviation of the AUV salinity observations. We denote the associated PDF by $p(\boldsymbol{y}_j|\boldsymbol{\xi})$.

Via Bayes' rule, data assimilation at stages $j = 1, \ldots J$, gives the sequential conditional PDF $p(\boldsymbol{\xi}|\mathcal{Y}_j) \propto p(\boldsymbol{y}_j|\boldsymbol{\xi})p(\boldsymbol{\xi}|\mathcal{Y}_{j-1})$. Under the assumptions about a GRF prior model and a Gaussian measurement error model, this conditional PDF is also Gaussian with mean $\boldsymbol{m}_j$ and covariance matrix $\boldsymbol{S}_j$ given by

$$\begin{aligned} \boldsymbol{G}_j &= \boldsymbol{S}_{j-1}\boldsymbol{F}_j^T(\boldsymbol{F}_j\boldsymbol{S}_{j-1}\boldsymbol{F}_j^T + \boldsymbol{R}_j)^{-1} \\ \boldsymbol{m}_j &= \boldsymbol{m}_{j-1} + \boldsymbol{G}_j(\boldsymbol{y}_j - \boldsymbol{F}_j\boldsymbol{m}_{j-1}) \\ \boldsymbol{S}_j &= \boldsymbol{S}_{j-1} - \boldsymbol{G}_j\boldsymbol{F}_j\boldsymbol{S}_{j-1}, \end{aligned} \tag{3}$$

where $\boldsymbol{m}_0 = \boldsymbol{\mu}$ and $\boldsymbol{S}_0 = \boldsymbol{\Sigma}$. The sequential updating resembles that of a spatio-temporal Kalman filter [27]. In our case, we study the benefits of using a 3D spatial model in the AUV sampling. Having a relatively short-term deployment, no explicit temporal dynamics are modeled.

B. Excursion Set and Expected Integrated Bernoulli Variance

We use the notion of an ES to characterize the river and ocean water masses [16]. The ES for salinity threshold t is defined by

$$\text{ES} = \{\boldsymbol{u} \in \mathcal{M} : \xi_{\boldsymbol{u}} \leq t\}. \tag{4}$$

Hence, salinity lower than this threshold will indicate river water. The associated excursion probability (EP) is

$$p_{\boldsymbol{u}} = P(\xi_{\boldsymbol{u}} \leq t), \qquad \boldsymbol{u} \in \mathcal{M}. \tag{5}$$

When it is close to 1 or 0 at a given location, it is easy to classify the water mass to be river or ocean respectively. EP close to 0.5 reflects ambiguity in the characterization of water masses. The prior Bernoulli variance (BV) at location $\boldsymbol{u}$ is $p_{\boldsymbol{u}}(1-p_{\boldsymbol{u}})$ and the spatially integrated BV (IBV) is

$$\text{IBV} = \int p_{\boldsymbol{u}}(1-p_{\boldsymbol{u}})d\boldsymbol{u}, \tag{6}$$

which is dominated by locations with probabilities near 0.5 and BV close 0.25. In practice the integral will be approximated by a sum over the n grid nodes.

The goal is to construct AUV sampling strategies that prioritize locations that are ambiguous, thus making the exploration more effective. At each stage, we define the EIBV by

$$\begin{aligned} \text{EIBV}(\boldsymbol{D}_j) &= \int E_{\boldsymbol{y}_j|\mathcal{Y}_{j-1};\boldsymbol{D}_j}\left[B_{\boldsymbol{u}}(\boldsymbol{y}_j)\right]d\boldsymbol{u}, \\ B_{\boldsymbol{u}}(\boldsymbol{y}_j) &= p_{\boldsymbol{u}}(\boldsymbol{y}_j,\boldsymbol{D}_j,\mathcal{Y}_{j-1})(1-p_{\boldsymbol{u}}(\boldsymbol{y}_j,\boldsymbol{D}_j,\mathcal{Y}_{j-1}), \end{aligned} \tag{7}$$

where $B_{\boldsymbol{u}}(\boldsymbol{y}_j)$ is the conditional Bernoulli variance for outcome $\boldsymbol{y}_j$ of data in design $\boldsymbol{D}_j$, and the conditional probability of an excursion is

$$p_{\boldsymbol{u}}(\boldsymbol{y}_j,\boldsymbol{D}_j,\mathcal{Y}_{j-1}) = P(\xi_{\boldsymbol{u}} \le t|\boldsymbol{y}_j,\boldsymbol{D}_j,\mathcal{Y}_{j-1}). \tag{8}$$

The notation in Equation (7) indicates that the EIBV is an expectation with respect to the random data $\boldsymbol{y}_j$ for design $\boldsymbol{D}_j$, conditional on the history of sampling results $\mathcal{Y}_{j-1}$.

The criterion for selecting design $\boldsymbol{D}_j$ and then getting data $\boldsymbol{y}_j$ at stage $j = 1,\ldots,J$, is based on the minimum EIBV computed for all designs in a candidate waypoint set denoted $\mathcal{D}_j$. We have

$$\boldsymbol{D}_j = \text{argmin}_{\boldsymbol{D}'_j \in \mathcal{D}_j}\text{EIBV}(\boldsymbol{D}'_j). \tag{9}$$

Using expressions similar to that of [28], the EIBV in Equation (7) can be evaluated in closed form. Denoting the variance reduction from data by $\boldsymbol{V}_j = \boldsymbol{G}_j\boldsymbol{F}_j\boldsymbol{S}_{j-1}$, see Equation (3), the EIBV becomes

$$\begin{aligned} \text{EIBV}(\boldsymbol{D}'_j) &= \sum_{i=1}^{n}\text{EBV}_{\boldsymbol{u}_i}(\boldsymbol{D}'_j) \\ \text{EBV}_{\boldsymbol{u}_i}(\boldsymbol{D}'_j) &= \Phi_2\left(\begin{bmatrix} t \\ -t \end{bmatrix};\begin{bmatrix} m_{j-1}(i) \\ -m_{j-1}(i) \end{bmatrix},\boldsymbol{W}_j(i,i)\right), \end{aligned} \tag{10}$$

where Φ_2 denotes the bivariate Gaussian cumulative distribution function, and with

$$\boldsymbol{W}_j(i,i) = \begin{bmatrix} T(i,i) & -V_j(i,i) \\ -V_j(i,i) & T(i,i) \end{bmatrix}, \quad T(i,i) = S_j(i,i) + V_j(i,i).$$

We next give some intuition for this EIBV criterion. Fig. 4 illustrates a Gaussian PDF (left) representing the current knowledge about salinity at some location. In this case it is standardized so that $Z_1 = \frac{\xi_{\boldsymbol{u}_i} - m_{j-1}(i)}{\sqrt{S_{j-1}(i,i)}}$ for location $\boldsymbol{u}_i$. The scaled threshold $t - m_{j-1}(i)$ is shown as a vertical

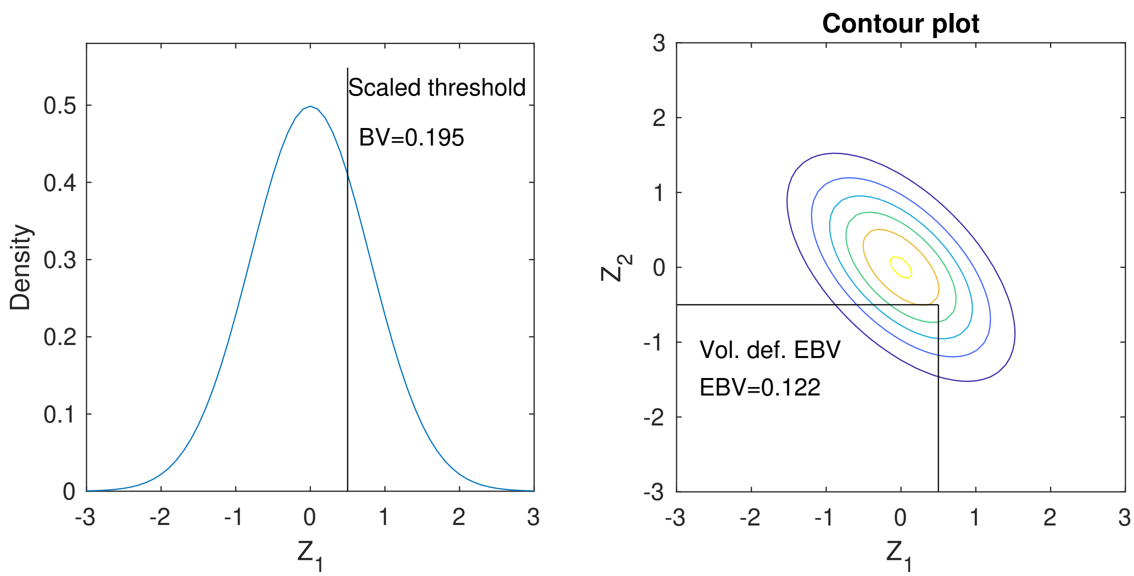

Fig. 4: Left: The density curve represents the current knowledge at a selected location, while the vertical line indicates the threshold. The Bernoulli variance (BV) is indicated. Right: The EBV calculation involves bivariate Gaussian cumulative probabilities, which is the volume below the contours in the bottom left region.

line. With variance $s_{j-1}^2(i) = S_{j-1}(i,i)$, the current BV $= p(1-p)$, $p = \Phi(\xi_{\boldsymbol{u}_i}; m_{j-1}(i), s_{j-1}^2(i))$ is also displayed.

We can collect data and get more information. The expected BV (EBV) at this location is then available as a cumulative probability as indicated in Fig. 4 (right). The EBV depends on the mean value relative to the threshold. Assume that the mean is lower, meaning that the threshold $t - m_{j-1}(i)$ moves to the right in the left display. Then the BV decreases, and the EBV illustrated in the right display also decreases as the vertical line moves right and the horizontal line moves down. The EBV is further smallest when there is much negative correlation in the density in Fig. 4 (right). From matrix $\boldsymbol{W}_j(i,i)$ in Equation (11), we see that this occurs when the variance reduction $V_j(i,i)$ is large compared with $S_j(i,i) + V_j(i,i)$. The bivariate Φ_2 calculation in Equation (10) is somewhat costly, and if the correlation term is small, one could approximate it with two univariate calculations to gain computational efficiency.

Previous research has demonstrated the possibility of using EIBV as the design criterion for AUV adaptive sampling in two-dimensional domains [16]. We next explain how we build on this to construct effective AUV operations in 3D adaptive sampling plans.

IV. Path planning algorithm

A. Adaptive sampling

The GRF model updating in Equation (3) and closed form EIBV calculation in Equation (10) enable information-based adaptive AUV sampling. We summarize the approach in Algorithm 1,

Algorithm 1 Informative myopic sampling algorithm

Initialization: $\boldsymbol{m}_0$, $\boldsymbol{S}_0$, t, $\mathcal{Y}_0 = \emptyset$, $\mathcal{D}_1$

$j = 1$

while $j \leq N_{steps}$ **do**

  Plan: Evaluate EIBV$(\boldsymbol{D}'_j)$ for all $\boldsymbol{D}'_j \in \mathcal{D}_j$ ▷ Eq. (7) and (10)

  $\boldsymbol{D}_j = \text{argmin}_{\boldsymbol{D}'_j \in \mathcal{D}_j} \text{EIBV}(\boldsymbol{D}'_j)$ ▷ Eq. (9)

  Go to design $\boldsymbol{D}_j$ with the AUV, set design matrix $\boldsymbol{F}_j$, form set $\mathcal{D}_{j+1}$.

  Sense: Gather in-situ AUV data $\boldsymbol{y}_j$ according to design $\boldsymbol{D}_j$.

  $\mathcal{Y}_j = (\mathcal{Y}_{j-1}, \boldsymbol{y}_j)$.

  Update : $\boldsymbol{G}_j = \boldsymbol{S}_{j-1}\boldsymbol{F}_j^T(\boldsymbol{F}_j\boldsymbol{S}_{j-1}\boldsymbol{F}_j^T + \boldsymbol{R}_j)^{-1}$

  $\boldsymbol{m}_j = \boldsymbol{m}_{j-1} + \boldsymbol{G}_j(\boldsymbol{y}_j - \boldsymbol{F}_j\boldsymbol{m}_{j-1})$, $\boldsymbol{S}_j = \boldsymbol{S}_{j-1} - \boldsymbol{G}_j\boldsymbol{F}_j\boldsymbol{S}_{j-1}$ ▷ Eq. (3)

  $j = j + 1$

end while

Note that as outlined this defines a myopic or greedy approach to adaptive sampling. This is not necessarily optimal. The myopic evaluation is done by taking the expectation of data at this stage only, without anticipation of what future sampling efforts might bring. The optimal solution to the sequential sampling design problem would also account for the sampling efforts at future stages. However, from the mathematical and computational setting, it is not feasible to find the optimal design strategy because it involves combinatorial growth of possible paths requiring intermixed optimization and expected values. Instead, one often resorts to the outlined myopic strategy. More nuanced approaches exist for doing longer-horizon search, for instance variants of

Markov Decision Processes (MDPs) or partially observed MDPs [29], rapidly-exploring random trees [30] or those based on genetic algorithms [31]. Such approaches will typically perform better than the myopic heuristic in situations with forbidden regions or with high collision risks, but it is not easy to use these in large-scale computations onboard the AUV. Further, restricted Monte Carlo search or pruning of paths, these non-myopic approaches will not necessarily improve performance compared with a myopic search on the regular waypoint graph case [16]. We will limit scope to the myopic calculations (Algorithm 1) in this work.

For the 3D application we consider here, the sequential sampling is restricted to a path embedded on a predefined grid of waypoints. In practice, the EIBV is computed for a set of neighborhood waypoint locations, meaning that the candidate design $\boldsymbol{D}_j'$ must be among those possible designs defining $\mathcal{D}_j$.

For small AUVs and large field, it might be possible to move the AUV wherever it needs to be. However, this might lead to an excess of manoeuvring time for the operation. To foster efficiency of the autonomous sampling process, a smooth-filtering method is applied to achieve AUV-friendly path planning (Algorithm 2). It firstly selects neighboring locations, and two vectors will be formed. Vector $\vec{b_1}$ is defined from the previous location to the current location, whereas vector $\vec{b_2}$ is from the current location to the potential candidate locations. Next, the inner products between there two vectors is calculated, and only candidate locations with positive inner products will be considered for EIBV evaluation.

A map view version of the smooth-filtering is depicted on a 2D waypoint graph in Fig. 5. In 3D, the principle is the same, except that it is expanded to include the vertical candidate

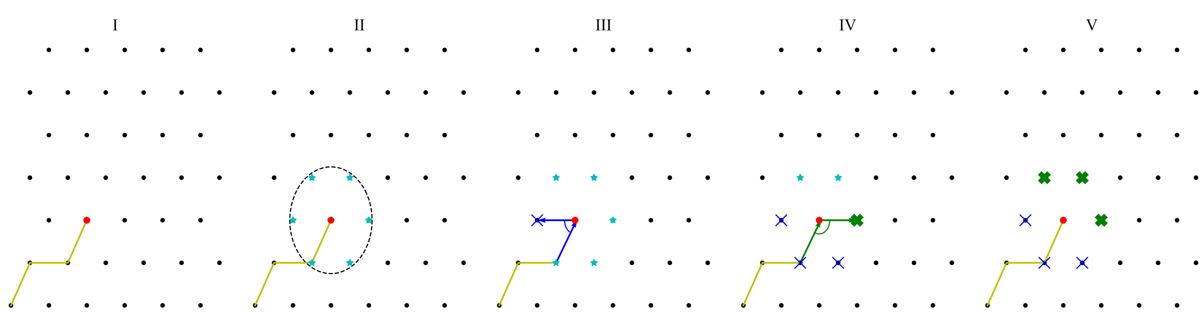

Fig. 5: Smooth path planning. I: arrive at the current location; II: search all neighboring locations; III, IV: compute inner products; V: select qualified candidate locations. Blue thin crosses indicate the abandoned locations, whereas the green thick crosses indicate the filtered locations.

Algorithm 2 Smooth-filtering algorithm

Require: $\boldsymbol{D}_{j-1}, \boldsymbol{D}_{j-2}$

$D^* = \{\boldsymbol{u} \in \mathcal{M}$ such that $|\boldsymbol{u} - \boldsymbol{D}_{j-1}| <$ neighboring distance$\}$

$\vec{b_1} = \boldsymbol{D}_{j-1} - \boldsymbol{D}_{j-2}$

$i = 1$

while $i \leq N_{\boldsymbol{D}^*}$ **do**

  $\vec{b_2} = \boldsymbol{D}^*_i - \boldsymbol{D}_{j-1}$

  if $\vec{b_1} \cdot \vec{b_2} < 0$ **then**

    Abandon $\boldsymbol{D}^*_i$.

  end if

  $i = i + 1$

end while

$\boldsymbol{D}_j = \boldsymbol{D}^*$

locations as well. This path smooth-filtering algorithm is effective since it removes locations which might require a hydrobatic maneuver to go there [32]. The smooth-filtered trajectory further avoids time-consuming turning which would increase the traveling time and introduce location inaccuracy.

V. Simulation study

To compare the performance between some existing algorithms and the 3D myopic algorithm that we have developed here, a simulation study is conducted. We next describe the case, present the various methods and discuss results.

A. *Simulation setup*

We use data from the numerical ocean model SINMOD as a reference for specifying realistic trends and variabilities for the oceanographic fjord-river water masses. Fig. 6 shows the average surface salinity field predicted for the first week in May using SINMOD. Four outlets from the river are recognized. The salinity variation from the river mouth to the ocean changes dramatically from bins of $[0, 3]$ to $[28, 30]$ ppt. The boundary between the freshwater and the more saline fjord water is clearly depicted by the contours.

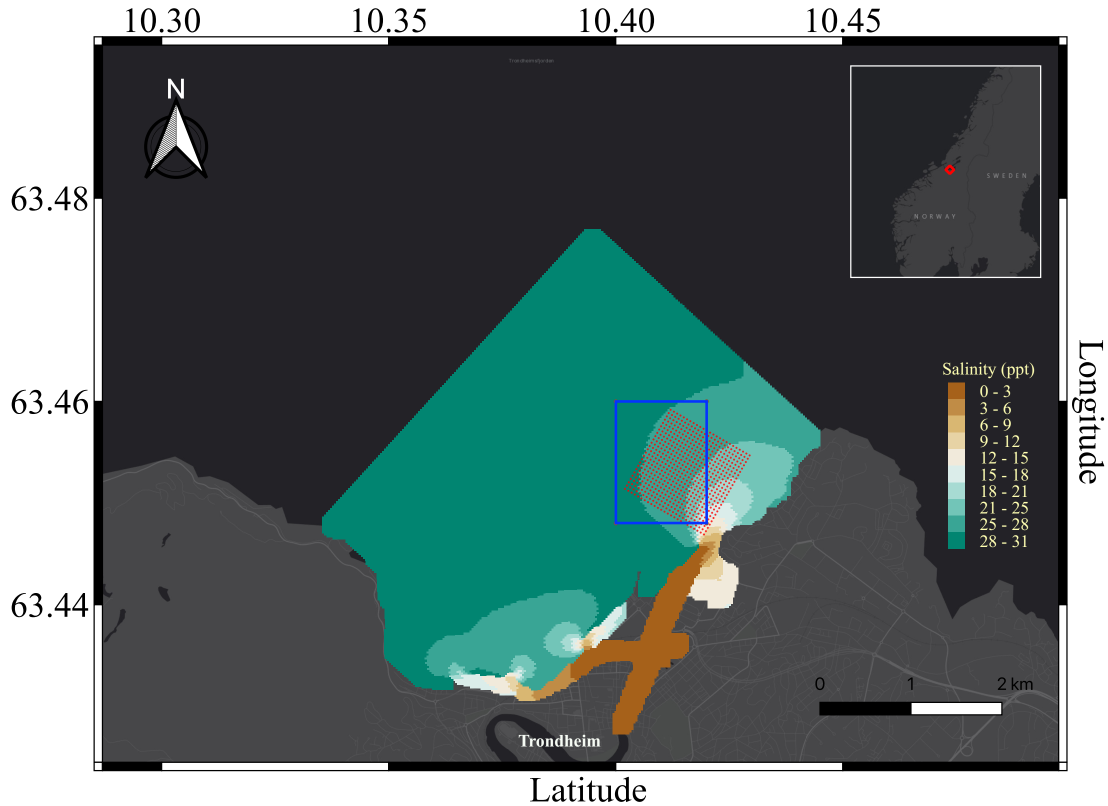

Fig. 6: Regional average surface salinity prediction in May 2021 from SINMOD. The blue rectangle indicates the designated simulation area (Section V), and the red dotted regions indicate the waypoint graph used in the field deployment (Section VI). The grid consists of 25×25 nodes in each lateral axis and 5 layers in depth. *Courtesy of SINTEF Ocean and ESRI basemap.*

To narrow down the focus on mapping the front of the river plume in 3D, a smaller region of interest in the easternmost part is selected (see blue rectangle in Fig. 6). Five depth layers 0.5m, 1.0m, 1.5m, 2.0m, 2.5m are used.

A 3D GRF benchmark field is created based on the data extracted from SINMOD on the desired simulation region. The mean values are set from averaging SINMOD data. The coefficients used in the Matérn covariance kernel are specified as $\sigma = 0.71$, $\phi_1 = 0.008$, $\phi_2 = 2.25$ and $r = 0.2$.

Fig. 7 shows one realization from our GRF model with the specified mean and covariance model. This is regarded as the ground truth in the simulation. There is clearly river plume areas to the south-east and near the surface, and realistic variability in salinity extent with some mixing

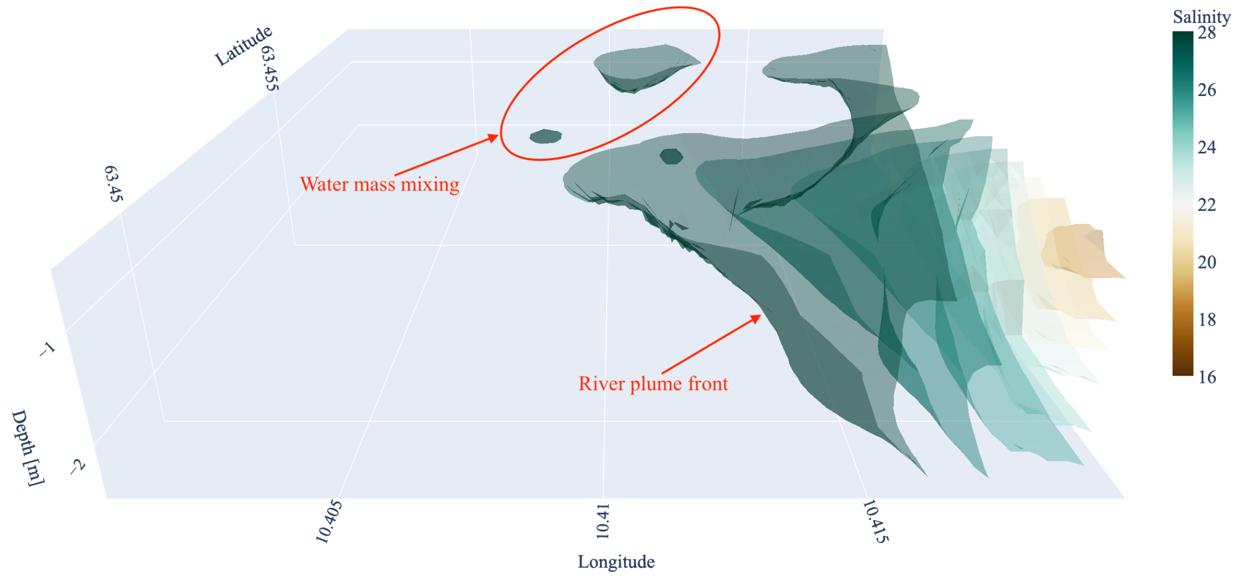

Fig. 7: One benchmark salinity field used in the simulation study. Some water blobs are shown on the north side of the region.

of water masses, indicating that the GRF model emulates the physical phenomenon rather well.

B. Simulation approaches

We next describe two additional sampling strategies that are compared with our suggested 3D adaptive sampling method. In all three, the GRF proxy model provides an easy way to update the knowledge of the field by measuring the data at specified locations. The differences occur in how the data is included in the on-board computing and in what sampling strategy is used to explore the domain. When we compare results of the various approaches, they will be influenced by the sampling methodology used.

1) Adaptive Myopic 2D: For the adaptive myopic 2D, the AUV is only moving adaptively in the middle layer with the myopic strategy. It updates the entire field based on the data obtained from the middle layer at $1.5m$ depth. In practice, the AUV needs to calibrate its navigational errors by constantly popping up onto the surface and request accurate GPS locations and dive back to the place where it should continue. This is achieved by a yoyo pattern, as shown in Fig. 8.

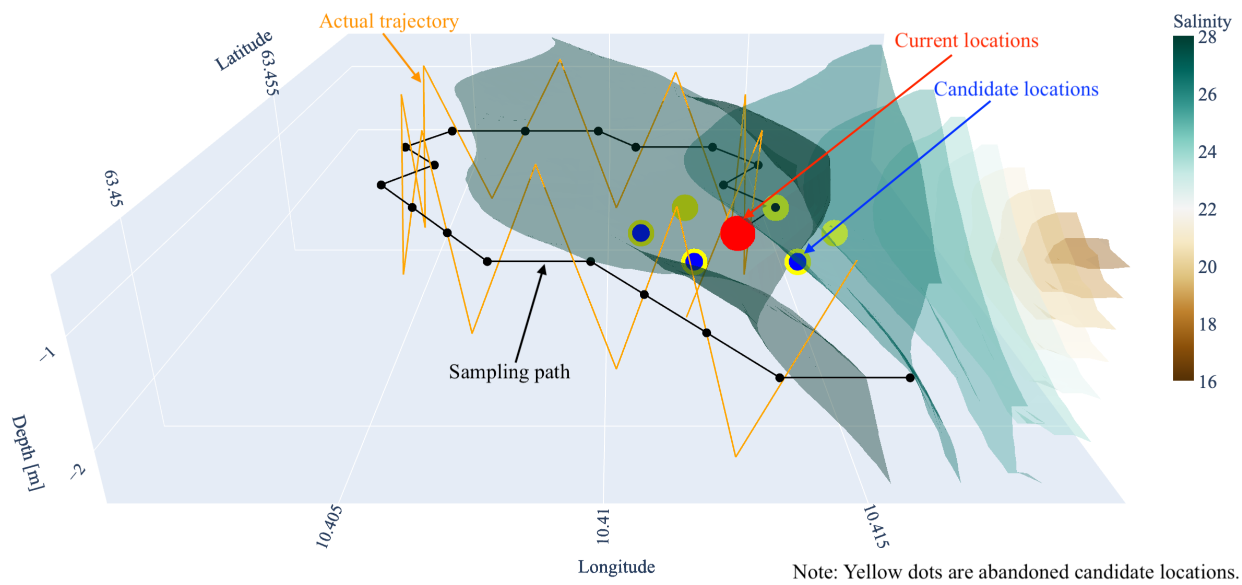

Fig. 8: Adaptive myopic 2D algorithm illustration. The outmost envelope shows the estimated boundary after sampling 20 locations. Note that the yoyo pattern is shown as an illustration. It can be denser in the actual setting.

2) Non-adaptive lawnmower: For the non-adaptive lawnmower, Fig. 9 shows that the AUV will follow a pre-designed 3D lawnmower pattern. In the lateral direction, the surface-projected trajectory will be a typical lawnmower manoeuvre. To extend it into 3D, a vertical yoyo manoeuvre is added in addition to the lateral lawnmower. This pre-programmed method requires no statistical computations at waypoints, and it uncovers the field with large coverage. But the approach is usually time-consuming and inefficient in finding interesting features as it does not adapt to the data.

3) Adaptive Myopic 3D: Our suggested adaptive myopic 3D strategy extends the potential candidate sampling locations from one layer to include multiple layers. Therefore, it adapts to the field data with a much wider perspective. It is further both energy-efficient and time-efficient. One example of the adaptive 3D myopic path planning is depicted in Fig. 10. One can see that at each stage, candidate locations will be generated in three dimensions. Only a few (shown as blue in Fig. 10) will be selected for the EIBV calculation due to the constraints of AUV maneuverability.

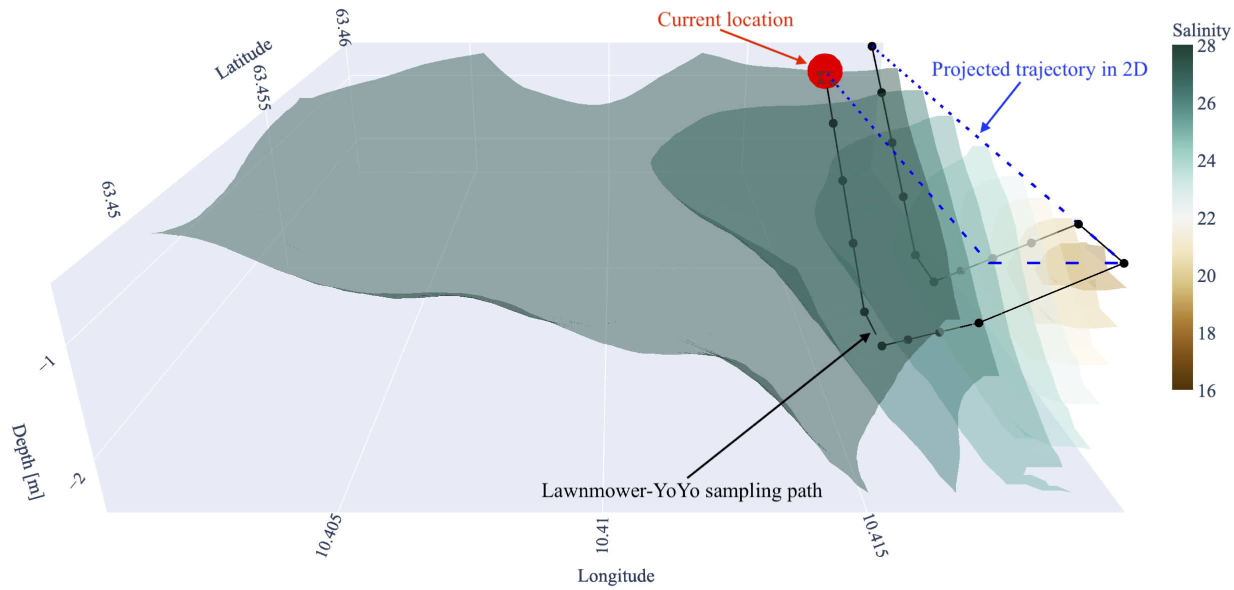

Fig. 9: Lawnmower-yoyo maneuver illustration. The estimated boundary after observing 20 sampling locations is shown as the outermost envelope.

C. Simulation results and discussion

Fig. 8∼10 show how each strategy behaves for one specific generated salinity field. To remove random effects, results of 100 replicate simulation results are averaged and shown in Fig. 11. At each time step of the runs, IBV (Integrated Bernoulli Variance), RMSE (Root Mean Squared Error), Variance reduction and Distance traveled are monitored for comparison of the three strategies.

The IBV indicator shows that the Lawnmower-yoyo pattern has the slowest reduction of the three strategies. However, it goes down quickly when the robot is in the area of interest, i.e., the boundary region or the front of the river plume, performing better than Myopic 2D after about 15 iterations (The same holds for RMSE and Variance reduction.) This occurs because the lawn mower strategy can get lucky and the AUV runs into interesting parts of the domain, but

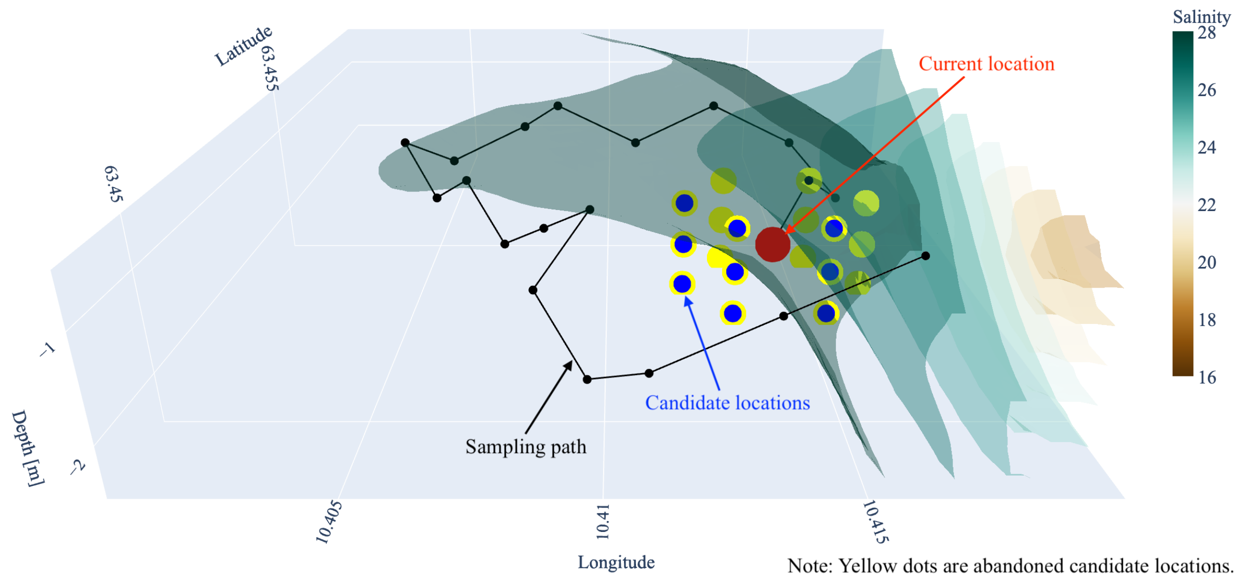

Fig. 10: Adaptive myopic 3D sampling illustration. The outermost envelope shows the estimated river plume front after sampling 20 locations with the adaptive myopic 3D path planning.

it can also miss this entirely in the given time window. Even though the Myopic 3D strategy is guided by EIBV reduction, it also achieves large reduction in RMSE and variance, and more so than the other methods. It performs better than the 3D Lawnmower strategy because it explores new parts of the domains and in doing so avoids locations that are highly correlated to the ones already sampled.

With the same starting location and about the same traveled distance (Fig. 11, lower right), the 3D version of the myopic planning reveals the most information of the field within the three strategies. The flexibility in 3D enables the AUV to both explore and exploit the environment effectively.

VI. AUV Experiments in the Nidelva plume

We next describe and show results of AUV experiments done in late Spring 2021 to map the Nidelva river plume, Trondheim, Norway. The adaptive AUV experiments were conducted on July 6th 2021. Before that, we gathered various complementary data. The phone footage on May 27th shows a visible river plume (Fig. 12). A satellite image on June 2nd (Fig. 13) shows how the river plume area is unfolded by pollen flushed away by the river in the spring season.

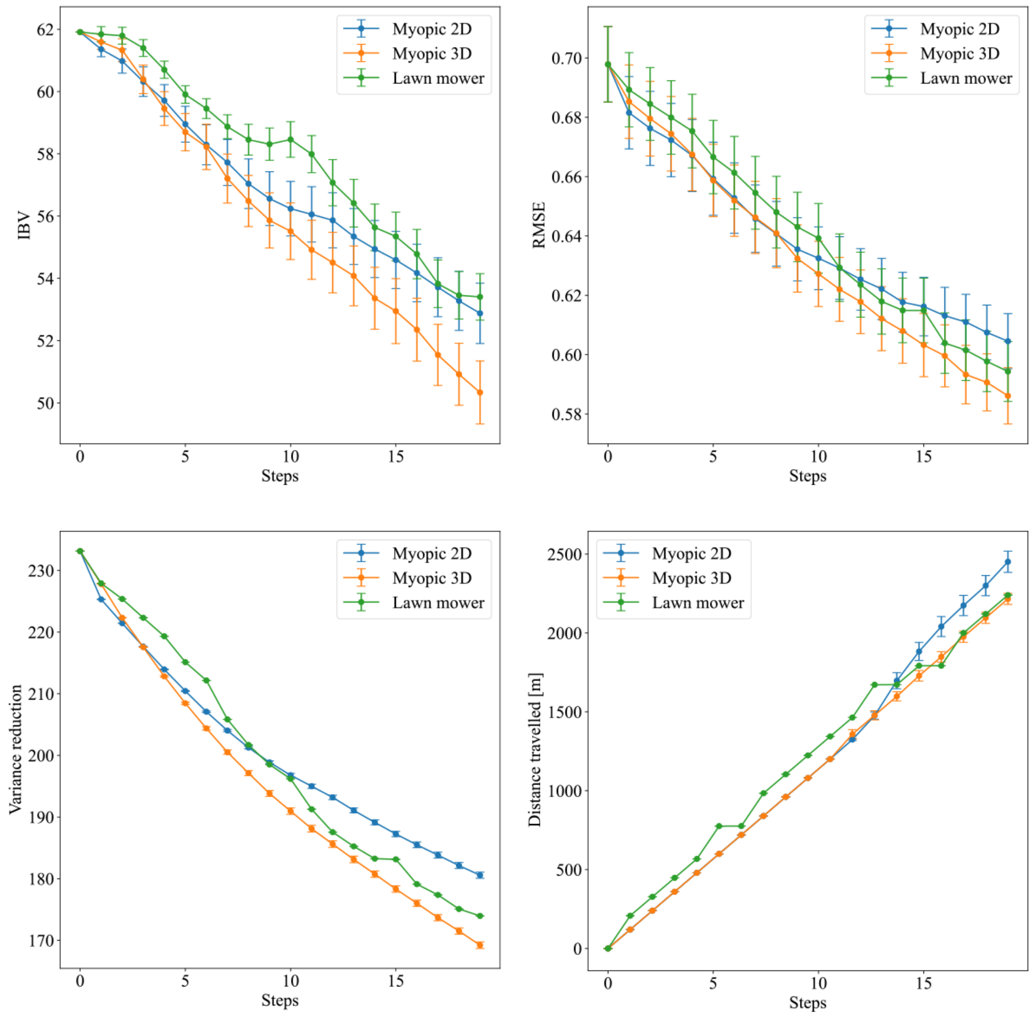

Fig. 11: Average results from 100 replicate simulations for 20 sampling locations. The standard error is depicted as vertical lines.

That matches very well with the phone footage (Fig. 12). Such data motivates AUV sampling for calibration, improved resolution and 3D characterization.

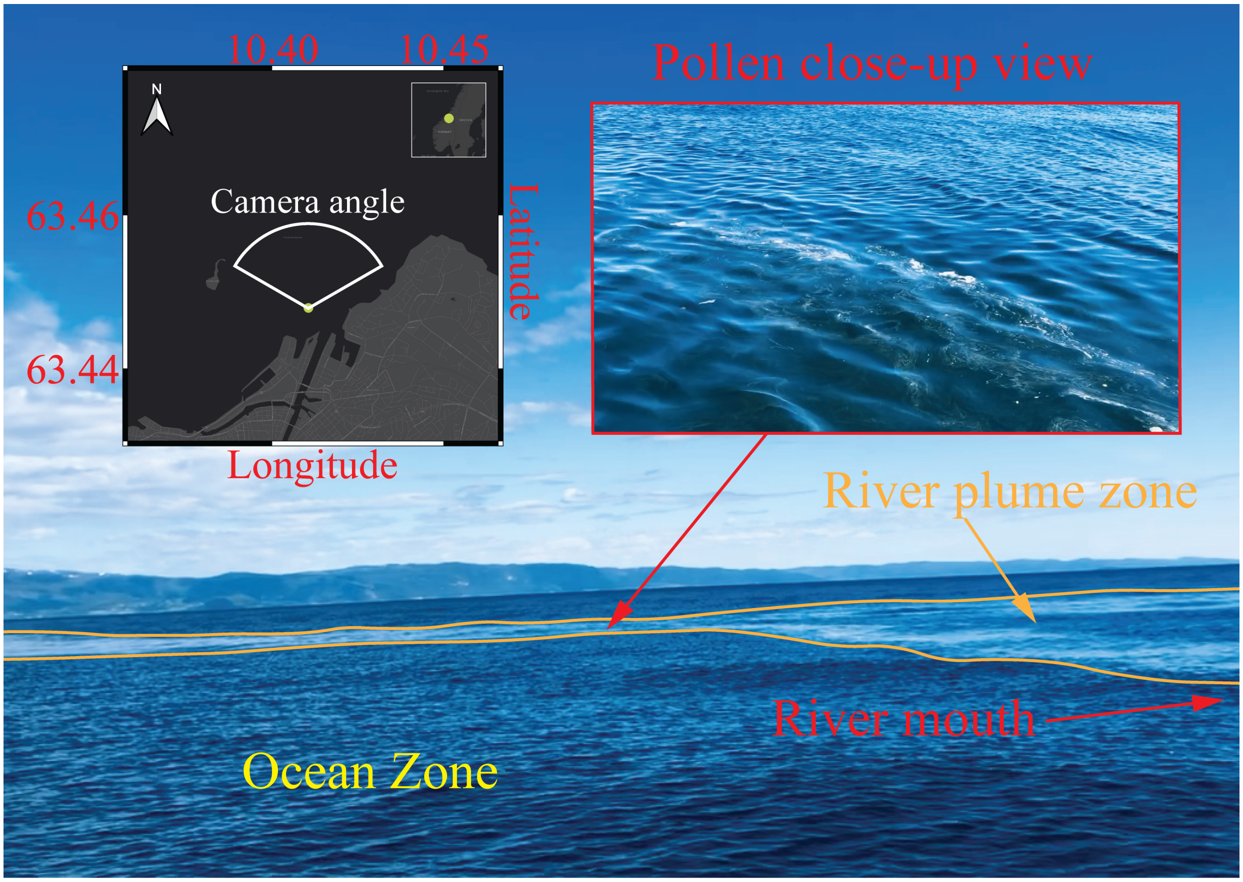

Fig. 12: River plume zone captured by the mobile phone on May 27th 2021. The camera perspective is shown as the white fan on the left corner which indicates the area where the plume occurs.

A. *Experiment setup*

1) Discretize the grid: Computational constraints and practical matters lead to a $25 \times 25 \times 5$ grid discretization within the $1km \times 1km \times 2m$ box region overlapping the river plume area as shown in Fig. 6 (red dots). We concentrate our effort on the near-surface regions (depth smaller than $2.5m$) because ocean model data and observations made during an initial AUV transect (Fig. 14) show that the freshwater river plume tends to float close to the surface regions [1].

2) Building the prior: To form a prior, we use SINMOD data as a core building block. First, we allocate mean values to each 3D grid node, extracted from averages over many SINMOD runs. Second, we calibrate these mean values in a regression model using AUV data from a preliminary transect survey. A linear regression model $y_{\boldsymbol{u}_k} = \beta_0 + \beta_1 y^{\text{SINMOD}}_{\boldsymbol{u}_k}$ is fitted, where

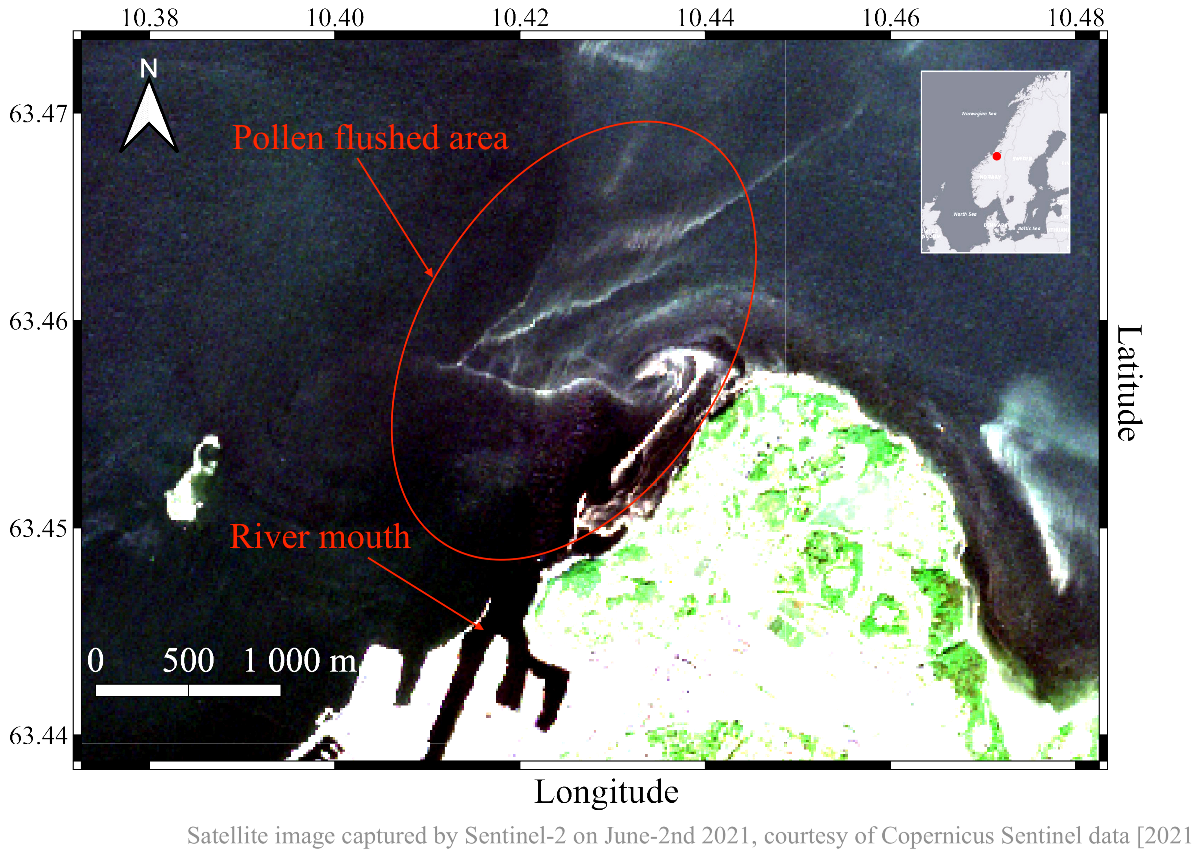

Fig. 13: Satellite image captured on 2 June 2021, showing the visible river plume thanks to the pollen flushed away by the river.

$\boldsymbol{u}_k$ indicate locations of transect line AUV data $y_{\boldsymbol{u}_k}$ and SINMOD data $y_{\boldsymbol{u}_k}^{\text{SINMOD}}$. The fitted coefficients $\hat{\beta}_0$, $\hat{\beta}_1$ adjust the entire field, and $\hat{\beta}_0 + \hat{\beta}_1 y_{\boldsymbol{u}_k}^{\text{SINMOD}}$ provides the prior mean in the onboard model used in the AUV deployment.

The coefficients for the Matérn kernel are approximated using empirical variograms of the AUV data collected from the initial survey. They are specified to $\sigma = 2$, $\phi_1 = 0.011$, $\phi_2 = 0.94$ and $r = 0.55$. Careful assessment of these parameters is important when it comes to sharpening the performance of the adaptive sampling algorithm such that it recognizes the boundary more agilely. However, further tweaking of these parameters are out of the scope of this work.

3) AUV deployment: LAUV Roald (Fig. 15) from the Applied Underwater Robotics Laboratory at NTNU was employed in the Nidelva missions. All the essential scripts were integrated onboard on the backseat NVIDIA Jetson TX2 CPU. For hardware and software in the loop testing and the actual deployment we relied on the framework developed by [12]. The implementation

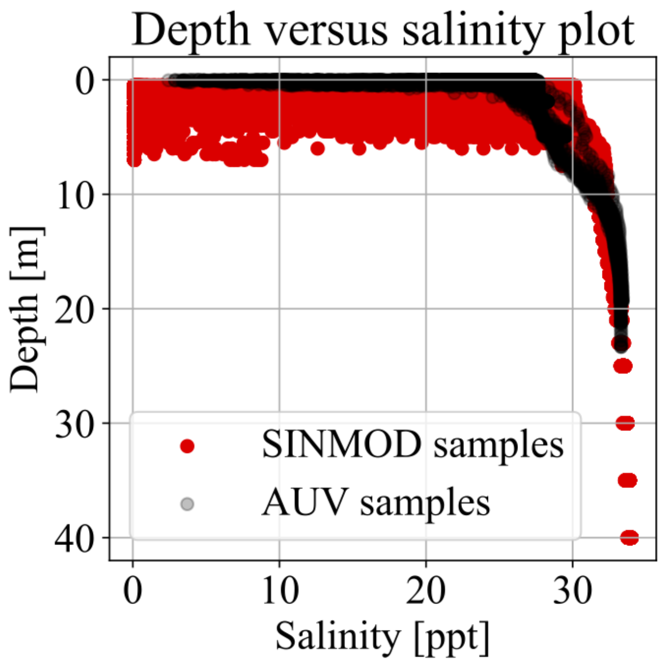

Fig. 14: Salinity versus depth plot from AUV in-situ measurements and from SINMOD prediction. Both SINMOD and the in-situ measurements show that most salinity variation happens close to the surface.

of Algorithm 1 and 2 requires Robot Operating Systems (ROS) [33] and a software bridge to the LAUV, running DUNE (DUNE :Unified Navigation Environment [34]) embedded and communicating over the Inter Module Communication (IMC) message protocol [35].

The software bridge between ROS and IMC was adapted from the Swedish Maritime Robotics Centers implementation of a ROS-IMC bridge [36] [1] to include messages going from ROS to the vehicle. In addition, a wrapper for the vehicle IMC messages was used, enabling easy interaction between the adaptive software and the vehicle. The communication bridge and framework between ROS and IMC use the same back-seat interface as [15], with IMC messages being transmitted over Transmission Control Protocol (TCP) [37] between the main CPU and the auxiliary CPU in the AUV. The adaptive code is run in the auxiliary CPU in order to preserve the integrity of the main CPU. For illustration, a flowchart containing the main software components

[1] https://github.com/smarc-project/imc_ros_bridge

Fig. 15: LAUV Roald is taking a shower after the heavy duty.

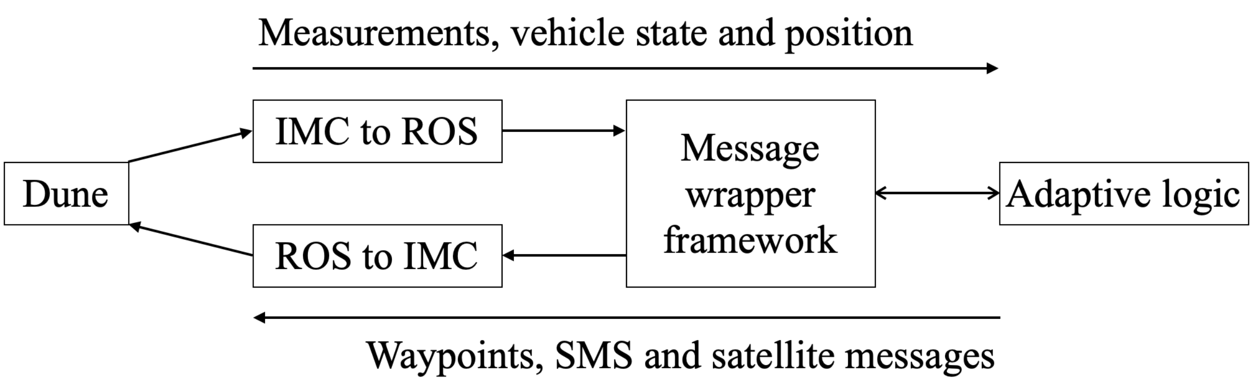

Fig. 16: Main software components in the communication between the adaptive code and the vehicle. DUNE [34] is running on the main CPU of the AUV while the IMC [35] messages are transmitted via TCP [37] to an auxiliary CPU, where ROS [33] and the adaptive code is run.

is presented in Fig. 16.

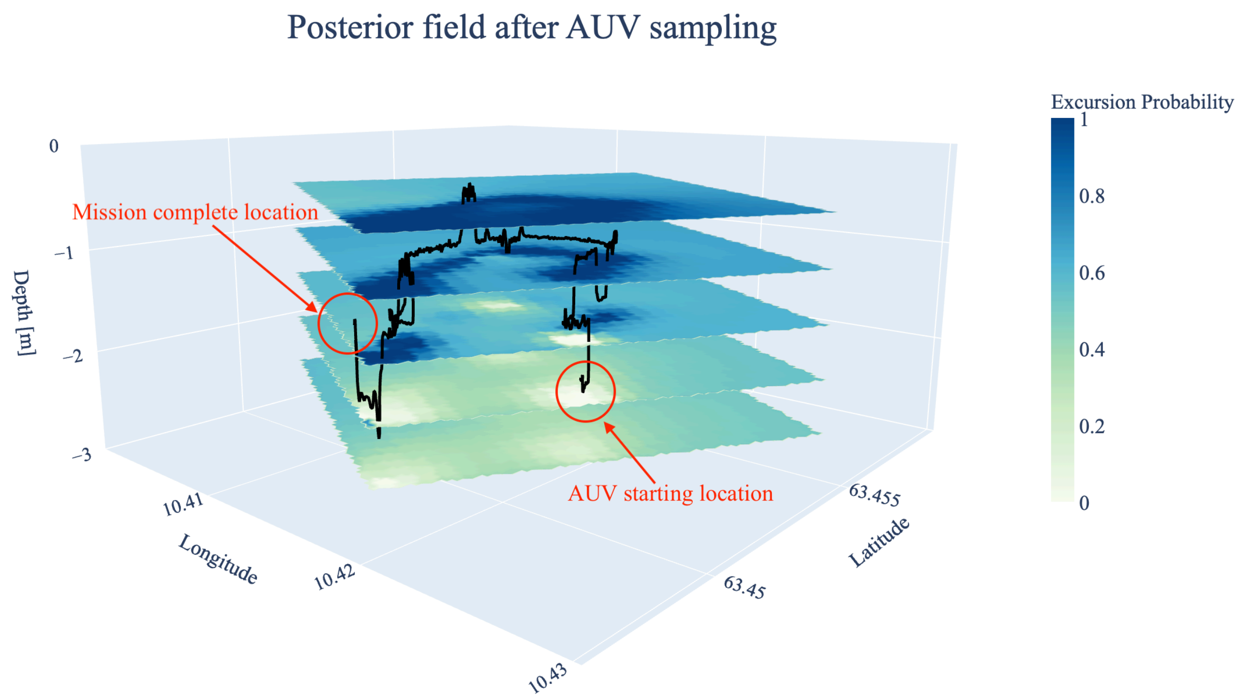

Fig. 17: Excursion probability for the posterior field. It describes how similar the water mass is to the river water. Values near 1 (blue) represents river water, while 0 (white) represents ocean water.

B. Experiment results and discussion

Fig. 17 shows the posterior EPs after assimilating all the AUV measurements from the adaptive mission. When the EP is close to 1, it is classified as river water, while ocean water has probabilities close to 0. Some parts of the domain are still unexplored and have intermediate probabilities. In its adaptive sampling efforts to distinguish the water masses, the AUV travels between different layers and traverse the lateral domain. The sampling mainly takes place in the top three layers that mirrors the buoyant river plume assumption, but it dips down to 2m and 2.5m. The adaptive behavior guides the agent to be within the boundary region instead of putting too much effort on either side of the front. According to the updated field, there appears to be patches of river waters going down to 1m and 1.5m, but most river water is near the surface.

In Fig. 18 we compare prior and posterior EPs for the top two layers. Clearly, the AUV reveals a bigger plume region than what is predicted by the SINMOD prior model. At 1.0 m there appears to be water mass separation. This kind of separation is likely very heterogeneous in space and time, and the displayed results only show predicted conditions at the day of the

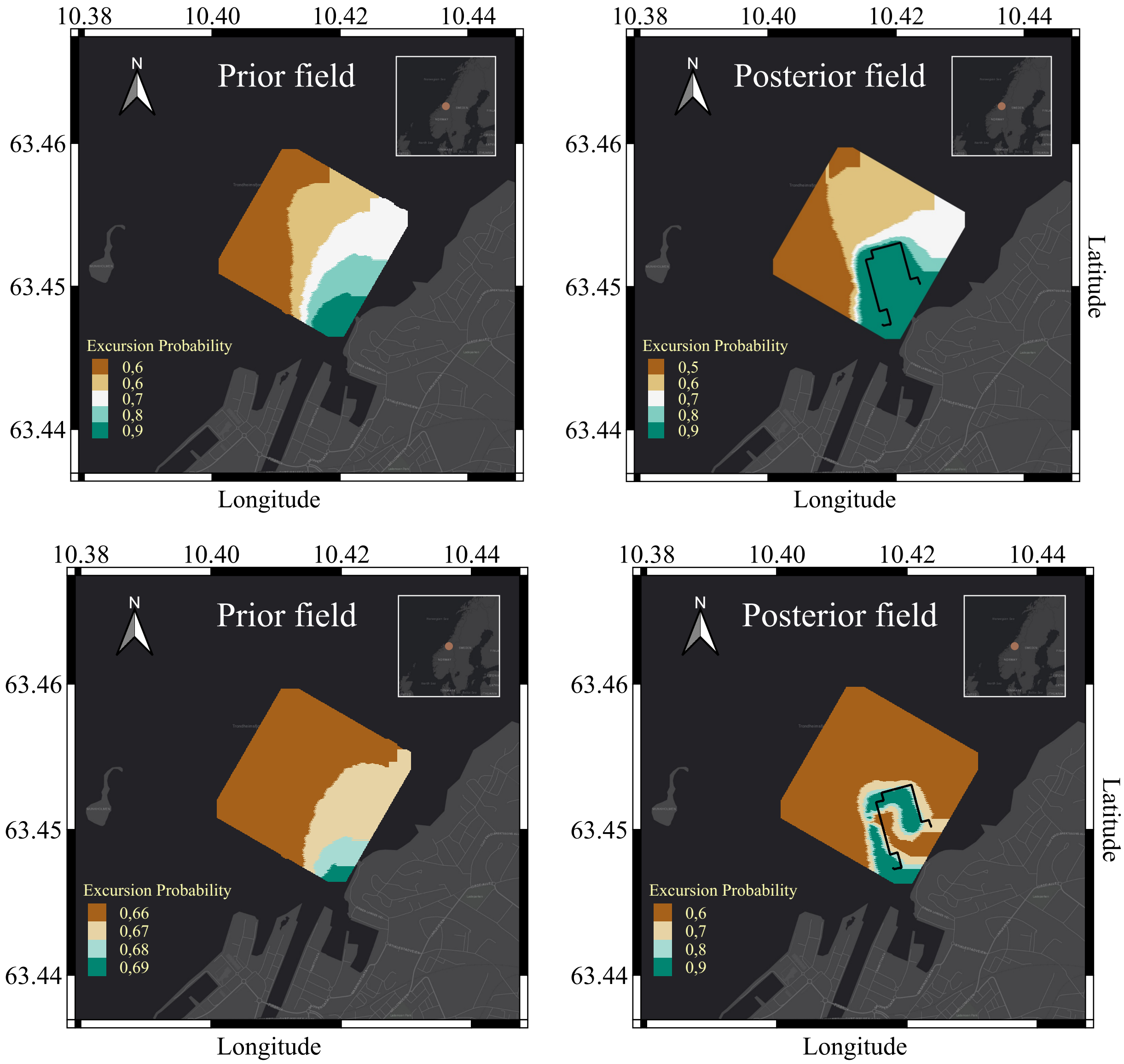

Fig. 18: Excursion probability comparison for the prior field (left) and the posterior field (right) at 0.5 m depth (top) and 1.0 m depth (bottom). The AUV trajectory is shown as the black line in the right column.

mission.

VII. Conclusion

The main contribution of this work is to apply Gaussian random field models for three-dimensional north-east-depth domains in the context of adaptive sampling with real-time computation and maneuverability routines on a robotic vehicle. The adaptive sampling routine presented here is tailored to frontal systems, and it relies on reduction of the expected integrated Bernoulli variance. We conducted a simulation study comparing the suggested approach with more standard approaches. Results demonstrate the capability of the adaptive myopic three dimensional sampling in a field deployment. The AUV managed to distinguish the different water masses in a river plume in a Norwegian fjord-river system.

River plumes are influenced by many factors such as winds, waves and tides, and we could likely model statistical correlations more sensibly by using a non-stationary Gaussian random field prior [38]. Our method uses ocean model data to build a reasonable prior model of the salinity field in 3D. However, when this type of information is lacking, the prior belief can also be constructed based on other data, possibly satellite imagery or buoy information. As AUV data are rather sparse, there is likely much to gain by using spatially covering physical modeling data and satellite data, as this allows a better initial model for sampling.

The time variation will play an important role if the AUV deployment lasts longer. This is naturally the case when the frontal region gets bigger and the distance traveled by the AUV increases. In long-term deployments it will also be important to capture such temporal effects [39]. The current myopic philosophy works well for a small river plume. As the plume gets bigger, or one has interest in capturing sub-regional plumes, there is likely some gain by using strategies that anticipate many stages [30, 31] or in using ocean physics for the three dimensional navigation [40]. Other opportunities stem from using adaptive sampling in a cooperative fleet as discussed in [41].

Acknowledgment

We acknowledge support from Norwegian Research Council (RCN) through the MASCOT project 305445. The authors thank AURLab NTNU for the support, collaboration, and easy access to testing equipment. We thank Kay Arne Skarpnes for his help during all the field-trials in 2021. We thank SINTEF Ocean for supplying SINMOD data.

References

[1] A. R. Horner-Devine, R. D. Hetland, and D. G. MacDonald, "Mixing and transport in coastal river plumes," *Annual Review of Fluid Mechanics*, vol. 47, no. 1, pp. 569–594, 2015.

[2] S. Constantin, D. Doxaran, and S. Constantinescu, "Estimation of water turbidity and analysis of its spatio-temporal variability in the danube river plume (black sea) using modis satellite data," *Continental Shelf Research*, vol. 112, pp. 14–30, 2016.

[3] A. A. Osadchiev and P. O. Zavialov, "Lagrangian model of a surface-advected river plume," *Continental Shelf Research*, vol. 58, pp. 96–106, 2013.

[4] S. Zheng, W. Guan, S. Cai, X. Wei, and D. Huang, "A model study of the effects of river discharges and interannual variation of winds on the plume front in winter in pearl river estuary," *Continental Shelf Research*, vol. 73, pp. 31–40, 2014.

[5] F. M. Falcieri, A. Benetazzo, M. Sclavo, A. Russo, and S. Carniel, "Po river plume pattern variability investigated from model data," *Continental Shelf Research*, vol. 87, pp. 84–95, 2014.

[6] R. Mendes, N. Vaz, D. Fernández-Nóvoa, J. Da Silva, M. Decastro, M. Gómez-Gesteira, and J. Dias, "Observation of a turbid plume using modis imagery: The case of douro estuary (portugal)," *Remote sensing of environment*, vol. 154, pp. 127–138, 2014.

[7] G. S. Saldías, J. L. Largier, R. Mendes, I. Pérez-Santos, C. A. Vargas, and M. Sobarzo, "Satellite-measured interannual variability of turbid river plumes off central-southern chile: Spatial patterns and the influence of climate variability," *Progress in Oceanography*, vol. 146, pp. 212–222, 2016.

[8] E. Park and E. M. Latrubesse, "Modeling suspended sediment distribution patterns of the amazon river using modis data," *Remote Sensing of Environment*, vol. 147, pp. 232–242, 2014.

[9] J. Hwang, N. Bose, and S. Fan, "Auv adaptive sampling methods: A review," *Applied Sciences*, vol. 9, no. 15, p. 3145, 2019.

[10] E. Fiorelli, N. E. Leonard, P. Bhatta, D. A. Paley, R. Bachmayer, and D. M. Fratantoni, "Multi-auv control and adaptive sampling in monterey bay," *IEEE Journal of Oceanic Engineering*, vol. 31, no. 4, pp. 935–948, 2006.

[11] T. O. Fossum, G. M. Fragoso, E. J. Davies, J. E. Ullgren, R. Mendes, G. Johnsen, I. Ellingsen, J. Eidsvik, M. Ludvigsen, and K. Rajan, "Toward adaptive robotic sampling of phytoplankton in the coastal ocean," *Science Robotics*, vol. 4, no. 27, p. eaav3041, 2019.

[12] T. Mo-Bjørkelund, T. O. Fossum, P. Norgren, and M. Ludvigsen, "Hexagonal grid graph as a basis for adaptive sampling of ocean gradients using auvs," in *Global Oceans 2020: Singapore – U.S. Gulf Coast*, 2020, pp. 1–5.

[13] P. Rogowski, E. Terrill, and J. Chen, "Observations of the frontal region of a buoyant river plume using an autonomous underwater vehicle," *Journal of Geophysical Research: Oceans*, vol. 119, no. 11, pp. 7549–7567, 2014.

[14] Y. Zhang, J. G. Bellingham, J. P. Ryan, B. Kieft, and M. J. Stanway, "Autonomous four-dimensional mapping and tracking of a coastal upwelling front by an autonomous underwater vehicle," *Journal of Field Robotics*, vol. 33, no. 1, pp. 67–81, 2016.

[15] J. Pinto, R. Mendes, J. C. B. da Silva, J. M. Dias, and J. B. de Sousa, "Multiple autonomous vehicles applied to plume detection and tracking," in *2018 OCEANS - MTS/IEEE Kobe Techno-Oceans (OTO)*, May 2018, pp. 1–6.

[16] T. O. Fossum, C. Travelletti, J. Eidsvik, D. Ginsbourger, and K. Rajan, "Learning excursion sets of vector-valued gaussian random fields for autonomous ocean sampling," *Annals of Applied Statistics*, vol. 15, no. 2, pp. 597–618, 2021.

[17] R. Cui, Y. Li, and W. Yan, "Mutual information-based multi-auv path planning for scalar field sampling using multidimensional rrt*," *IEEE Transactions on Systems, Man, and Cybernetics: Systems*, vol. 46, no. 7, pp. 993–1004, 2016.

[18] P. Stankiewicz, Y. T. Tan, and M. Kobilarov, "Adaptive sampling with an autonomous underwater vehicle in static marine environments," *Journal of Field Robotics*, vol. 38, no. 4, pp. 572–597, 2021.

[19] A. Sousa, L. Madureira, J. Coelho, J. Pinto, J. Pereira, J. B. Sousa, and P. Dias, "Lauv: The man-portable autonomous underwater vehicle," *IFAC Proceedings Volumes*, vol. 45, no. 5, pp. 268–274, 2012.

[20] D. Slagstad and T. A. McClimans, "Modeling the ecosystem dynamics of the barents sea including the marginal ice zone: I. physical and chemical oceanography," *Journal of Marine Systems*, vol. 58, no. 1-2, pp. 1–18, 2005.

[21] P. F. Lermusiaux, "Uncertainty estimation and prediction for interdisciplinary ocean dynamics," *Journal of Computational Physics*, vol. 217, no. 1, pp. 176–199, 2006.

[22] M. Lin and C. Yang, "Ocean observation technologies: A review," *Chinese Journal of Mechanical Engineering*, vol. 33, no. 1, pp. 1–18, 2020.

[23] S. Martin, *An introduction to ocean remote sensing*. Cambridge University Press, 2014.

[24] F. A. Al-Wassai and N. V. Kalyankar, "Major limitations of satellite images," 2013.

[25] S. Kemna, O. Kroemer, and G. S. Sukhatme, "Pilot surveys for adaptive informative sampling," in *2018 IEEE International Conference on Robotics and Automation (ICRA)*,

2018, pp. 6417–6424.

[26] F. S. Longman, L. Mihaylova, and L. Yang, “A gaussian process regression approach for fusion of remote sensing images for oil spill segmentation,” in *2018 21st International Conference on Information Fusion (FUSION)*, 2018, pp. 62–69.

[27] N. Cressie and C. K. Wikle, *Statistics for spatio-temporal data*. John Wiley & Sons, 2015.

[28] C. Chevalier, J. Bect, D. Ginsbourger, E. Vazquez, V. Picheny, and Y. Richet, “Fast parallel kriging-based stepwise uncertainty reduction with application to the identification of an excursion set,” *Technometrics*, vol. 56, no. 4, pp. 455–465, 2014.

[29] D. Silver and J. Veness, “Monte-carlo planning in large pomdps,” *Advances in neural information processing systems*, vol. 23, 2010.

[30] C. Xiong, H. Zhou, D. Lu, Z. Zeng, L. Lian, and C. Yu, “Rapidly-exploring adaptive sampling tree*: A sample-based path-planning algorithm for unmanned marine vehicles information gathering in variable ocean environments,” *Sensors*, vol. 20, no. 9, p. 2515, 2020.

[31] M. Bresciani, F. Ruscio, S. Tani, G. Peralta, A. Timperi, E. Guerrero-Font, F. Bonin-Font, A. Caiti, and R. Costanzi, “Path planning for underwater information gathering based on genetic algorithms and data stochastic models,” *Journal of Marine Science and Engineering*, vol. 9, no. 11, p. 1183, 2021.

[32] S. Bhat, “Hydrobatics: Efficient and agile underwater robots,” Ph.D. dissertation, KTH Royal Institute of Technology, 2020.

[33] M. Quigley, “Ros: an open-source robot operating system,” in *ICRA 2009*, 2009.

[34] J. Pinto, P. S. Dias, R. Martins, J. Fortuna, E. Marques, and J. Sousa, “The lsts toolchain for networked vehicle systems,” in *2013 MTS/IEEE OCEANS - Bergen*, 2013, pp. 1–9.

[35] LSTS. (2022) Inter module communication protocal. [Online]. Available: https://lsts.pt/docs/imc/master

[36] S. Bhat, I. Torroba, Ö. Özkahraman, N. Bore, C. I. Sprague, Y. Xie, I. Stenius, J. Severholt, C. Ljung, J. Folkesson *et al.*, “A cyber-physical system for hydrobatic auvs: system integration and field demonstration,” in *2020 IEEE/OES Autonomous Underwater Vehicles Symposium (AUV)*. IEEE, 2020, pp. 1–8.

[37] V. Cerf and R. Kahn, “A protocol for packet network intercommunication,” *IEEE Transactions on Communications*, vol. 22, no. 5, pp. 637–648, 1974.

[38] G.-A. Fuglstad, F. Lindgren, D. Simpson, and H. Rue, “Exploring a new class of non-

stationary spatial gaussian random fields with varying local anisotropy," *Statistica Sinica*, pp. 115–133, 2015.

[39] K. H. Foss, G. E. Berget, and J. Eidsvik, "Using an autonomous underwater vehicle with onboard stochastic advection-diffusion models to map excursion sets of environmental variables," *Environmetrics*, p. e2702, 2022.

[40] C. S. Kulkarni and P. F. Lermusiaux, "Three-dimensional time-optimal path planning in the ocean," *Ocean Modelling*, vol. 152, p. 101644, 2020.

[41] M. J. Kuhlman, D. Jones, D. A. Sofge, G. A. Hollinger, and S. K. Gupta, "Collaborating underwater vehicles conducting large-scale geospatial tasks," *IEEE Journal of Oceanic Engineering*, vol. 46, no. 3, pp. 785–807, 2021.